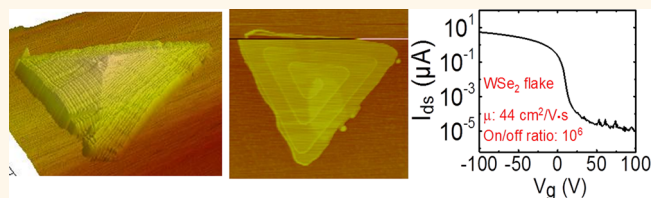


Screw-Dislocation-Driven Growth of Two-Dimensional Few-Layer and Pyramid-like WSe₂ by Sulfur-Assisted Chemical Vapor Deposition

Liang Chen,[†] Bilu Liu,[†] Ahmad N. Abbas, Yuqiang Ma, Xin Fang, Yihang Liu, and Chongwu Zhou*

Department of Electrical Engineering, University of Southern California, Los Angeles, California 90089, United States. [†]Equal contribution.

ABSTRACT Two-dimensional (2D) layered tungsten diselenides (WSe₂) material has recently drawn a lot of attention due to its unique optoelectronic properties and ambipolar transport behavior. However, direct chemical vapor deposition (CVD) synthesis of 2D WSe₂ is not as straightforward as other 2D materials due to the low reactivity between reactants in WSe₂ synthesis. In addition, the growth mechanism of WSe₂ in such CVD process remains unclear. Here we report the observation of a screw-dislocation-driven (SDD) spiral growth of 2D WSe₂ flakes and pyramid-like structures using a sulfur-assisted CVD method. Few-layer and pyramid-like WSe₂ flakes instead of monolayer were synthesized by introducing a small amount of sulfur as a reducer to help the selenization of WO₃, which is the precursor of tungsten. Clear observations of steps, helical fringes, and herringbone contours under atomic force microscope characterization reveal the existence of screw dislocations in the as-grown WSe₂. The generation and propagation mechanisms of screw dislocations during the growth of WSe₂ were discussed. Back-gated field-effect transistors were made on these 2D WSe₂ materials, which show on/off current ratios of 10⁶ and mobility up to 44 cm²/(V·s).



KEYWORDS: tungsten diselenides · WSe₂ · screw dislocation · two-dimensional layered materials · transition metal dichalcogenides · TMDC · chemical vapor deposition

Recently, two-dimensional (2D) layered materials beyond graphene have attracted huge amounts of attention especially for those transition metal dichalcogenides (TMDCs) with formula of MX₂ (M = Mo, W; X = S, Se).^{1–4} Such TMDCs are also layered materials like graphene coupled by weak van der Waals forces between adjacent layers. But more than that, each TMDC layer contains three covalent bonded X–M–X atomic layers. Besides the unique structure, these materials exhibit interesting properties when the thickness goes down to monolayer or few-layers,^{2,5–7} making them good candidates for advanced electronics,^{8–11} optoelectronic devices,^{12–15} energy storage devices,¹⁶ and electrocatalysts.¹⁷ So far, myriad research efforts have been devoted to these materials focusing on material synthesis,^{2,18–23} characterization,^{24,25} fundamental property studies,^{4,26–28} and applications.^{11–15,29,30} Among those four materials (MoS₂, MoSe₂, WS₂, and WSe₂), MoS₂ is the most heavily studied one. On the other

hand, WSe₂ has not been well studied until some recent papers.^{13–15} Compared to MoS₂, WSe₂ possesses a smaller band-gap and it exhibits ambipolar transport phenomenon.^{13–15}

Chemical vapor deposition (CVD) is a widely used method for TMDC synthesis.^{18–21} Early in 2012, Balendhran and Kalantar-zadeh *et al.* have shown the preparation of thin MoS₂ flakes by evaporation of sulfur and MoO₃, followed by exfoliation.³¹ Although CVD growth of MoS₂ has been well developed, only a few papers reported the successful growth of 2D WSe₂ structures.^{32–34} The difficulty of CVD growth of WSe₂ is believed to originate from the low reactivity of selenium.^{20,32} For example, Huang *et al.* have reported the synthesis of large area monolayer WSe₂ on sapphire under low-pressure CVD, and they found that adding H₂ as an additional reducing reactant is a must for successful WSe₂ synthesis.³² Few-layer WSe₂ synthesis was also reported recently by Lin *et al.* using graphene as an

* Address correspondence to chongwuz@usc.edu.

Received for review August 25, 2014 and accepted October 15, 2014.

Published online 10.1021/nn504775f

© XXXX American Chemical Society

epitaxial substrate.³⁴ Nevertheless, the growth mechanism of WSe_2 is still not clear. And more efforts should be devoted to further explore the controlled synthesis of WSe_2 . Here we report a sulfur-assisted CVD method to grow few-layer and pyramid-like WSe_2 flakes following a screw-dislocation-driven (SDD) growth fashion. Such SDD growth is a universal growth mechanism in nanomaterials including 1D nanotubes,^{35,36} 1D nanowires,^{37–39} and 2D nanoplates.^{40,41} However, it has not been reported in CVD synthesis of 2D layered materials. We believe this unique growth process in our method is due to low concentration of the reactants, and accordingly, relevant models are proposed to understand the SDD growth process in the CVD synthesis of WSe_2 flakes.

RESULTS AND DISCUSSIONS

Figure 1a illustrates the CVD setup we used for the synthesis of few-layer and pyramid-like WSe_2 flakes in this study. Similar to recent CVD methods for TMDC synthesis,^{30,32} a quartz boat containing WO_3 powders with a Si/SiO₂ substrate sitting on top was placed in the middle of a 1-in. tube furnace. The temperature of WO_3 varied from 875 to 925 °C. Selenium and sulfur powders were loaded in two separated quartz boats and put at the upstream region. Note that only very small amounts of sulfur powders were used and they were

intentionally put at a position with temperature below the melting point of sulfur to minimize their sublimation. After the growth, the SDD grown flakes can be found everywhere on the substrate. But the nucleation density is higher at positions closer to the WO_3 powders. More experimental details can be found in the Methods section.

When the growth temperature and time were adjusted, a variety of WSe_2 flakes with different thicknesses and morphologies were synthesized (Figure 1b–m), including few-layer triangles, few-layer hexagons, thick triangles, and thick hexagons. Figure 1b–d shows optical microscopy images of thin flakes synthesized at temperatures ranging from 875 to 900 °C. Besides the triangular and merged triangular flakes that are commonly observed in CVD-grown TMDCs,²⁵ hexagonal flakes are also occasionally found here. The lateral sizes of these flakes are ranging from 3 to 5 μm . When the growth temperature increased to 925 °C, we found that the flakes were predominantly thick ones based on optical microscopy observations. This is consistent with recent results showing that additional layers would grow at high temperature during CVD synthesis of MoS_2 and WSe_2 .^{32,42} In our experiments, we found that the growth window of WSe_2 is narrow, and temperature plays the most important role in determining the thickness and shape

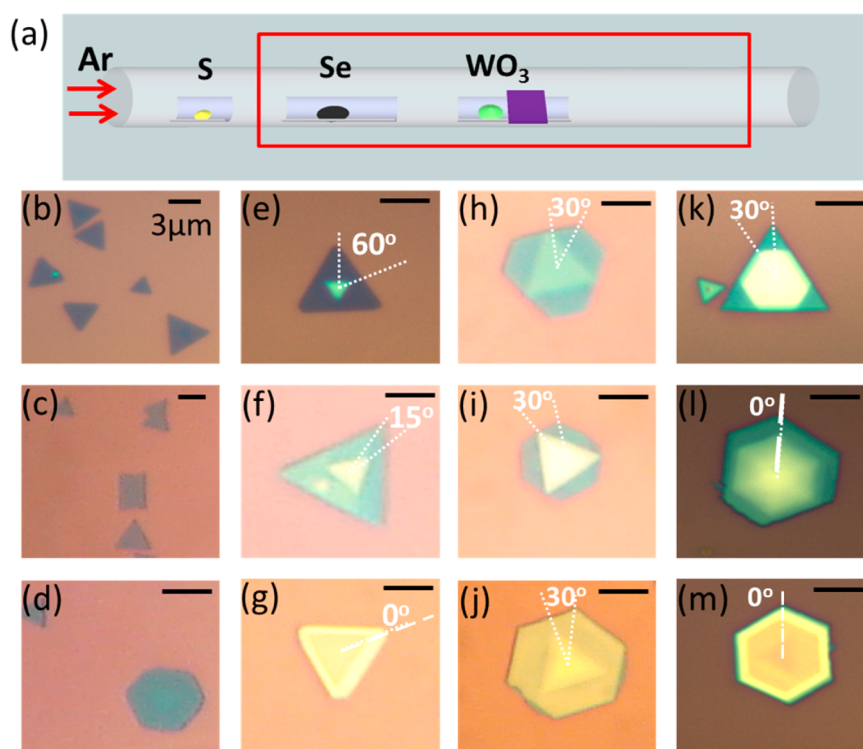


Figure 1. CVD setup and optical microscopy characterization of CVD-grown few-layer and pyramid-like WSe_2 flakes. (a) A schematic diagram shows the CVD setup for the sulfur-assisted WSe_2 growth. (b–d) Optical microscopy images of thin WSe_2 flakes with different shapes. (e–m) Optical microscopy images of thick WSe_2 flakes with different stacking morphologies. The color contrasts reflect the thickness variations both from sample to sample and from center to edge within each sample. The white dotted lines indicate the stacking angles between top and bottom features in thick flakes. The scale bars are 3 μm for all images.

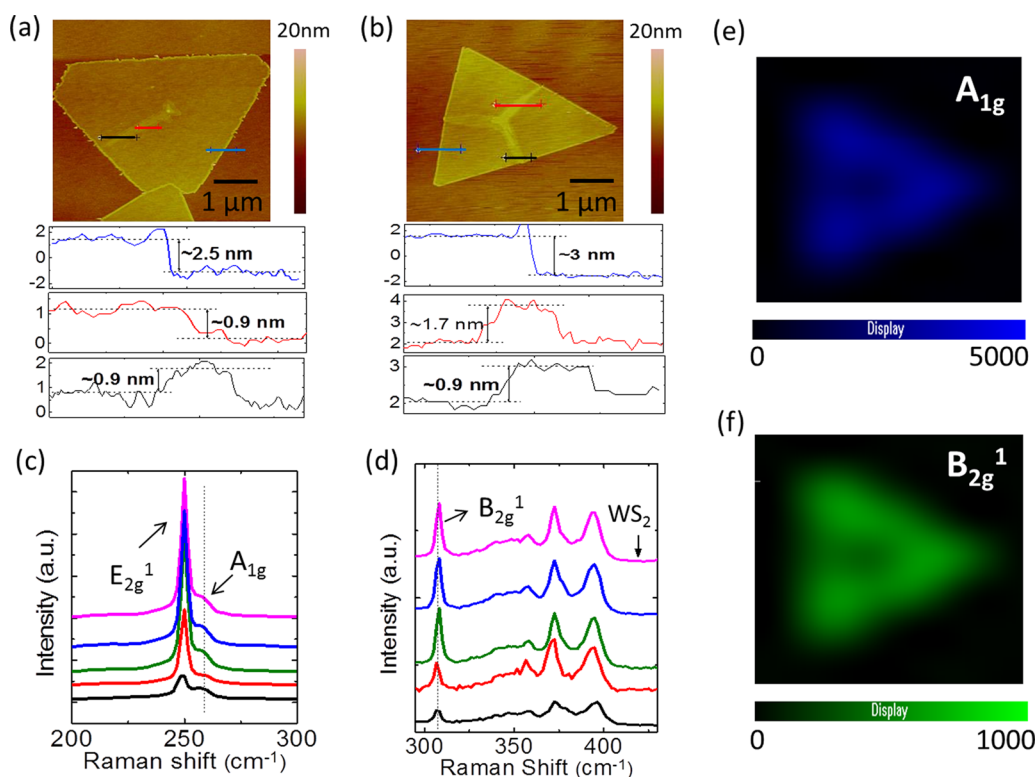


Figure 2. AFM and Raman characterization of thin WSe₂ flakes. (a and b) AFM images along with cross section height profiles of two thin WSe₂ flakes with ribbon-like features on top. The bottom layers are 2.5 and 3 nm in height, corresponding to around trilayer WSe₂. The heights of ribbon layers are ~ 0.9 or ~ 1.7 nm, corresponding to one or two layers of WSe₂. (c and d) Raman spectra of several thin WSe₂ flakes. Characteristic peaks of E_{2g}¹, A_{1g}, and B_{2g}¹ modes of WSe₂ were detected, while the A_{1g} peak of WS₂ was not observed. (e and f) Raman intensity mapping of A_{1g} (259 cm⁻¹) and B_{2g}¹ peaks (309 cm⁻¹) of the same WSe₂ flake shown in panel b. The excitation wavelength of laser is 532 nm during Raman measurements.

of the materials. In general, both thin and thick flakes coexist at a temperature of 900 °C (Supporting Information Figure S1a), while at relative high temperatures (above 925 °C), all the flakes are thick ones with heights over 10 nm (Supporting Information Figure S1b). We did a statistical analysis of the samples grown at 900 °C based on Supporting Information Figure S1a, and the results show that 78% are thin flakes and 22% are thick flakes (>10 nm). Temperature also plays a crucial role in affecting the shapes of as-grown materials. Most flakes are triangular when the growth temperature is below 900 °C. After the growth temperature rises to 925 °C, both triangular flakes and hexagonal flakes exist. Statistical studies on the samples grown at 925 °C shows that 96% are triangular and 4% are hexagonal. We note that this ratio may vary from location to location on a substrate. Very interestingly, most thick WSe₂ flakes in our products have intriguing terrace-like morphologies with different stacking angles and shapes, as exhibited from Figure 1e–m. The color contrasts of these images in Figure 1 reflect the differences of thickness among the WSe₂ samples. On the basis of the optical microscope inspections, the thicknesses of these thick flakes decrease from centers to edges, indicating the formation of pyramid-like structures. To be noticed, although Figure 1 shows all possible morphologies observed

during the experiments, some stacking types do appear more frequently than others. Detailed results will be discussed later.

To further explore the detailed structures of thin and stacked thick WSe₂ flakes, we performed systematical atomic force microscopy (AFM) and Raman studies. AFM characterization shows that most of the thin flakes (Figure 1b–d) are few-layer materials, such as trilayers (Figure 2a,b) and four-layers (Supporting Information Figure S2), as evident from the cross-section height profiles (bottom parts of Figure 2a,b). More importantly, we frequently observed that there are ribbon-like features lying on top of these thin flakes (Supporting Information Figure S3). The ribbons usually have heights equal to one or two-layer thickness of WSe₂ (red and black height profiles in Figure 2a,b). Figure 2c,d shows Raman spectra taken from several such thin flakes. Two characteristic peaks were observed in the region from 245 to 260 cm⁻¹, which can be assigned to E_{2g}¹ and A_{1g} modes of WSe₂, respectively.^{43–45} For few-layer WSe₂, these two peaks are very close to each other and thickness-dependent shift of Raman peak position is relatively small comparing to MoS₂.^{43,46} Therefore, it is difficult to use the peak-to-peak distance to precisely determine the layer numbers. Nevertheless, the existence of B_{2g}¹ peaks at 309 cm⁻¹ reveals that they are few-layer flakes,^{44,45} which is consistent with

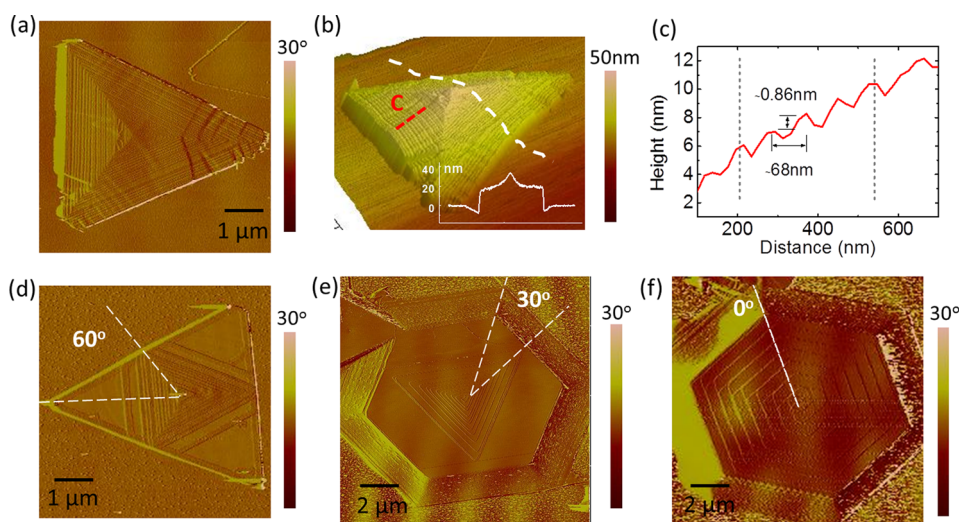


Figure 3. AFM studies of thick WSe₂ flakes with different stacking morphologies. (a) AFM phase image of a thick triangular flake. Helical fringes and herringbone contours are clearly observed. (b) A 3D AFM image of the flake in (a), showing a pyramid-like structure vividly with a height of ~40 nm from base to the summit. (c) AFM height profile of the pyramid-like flake along the red line in (b). (d–f) AFM phase images of three other thick flakes with different morphologies.

AFM measurements shown above. Moreover, there is no peak found at $\sim 420\text{ cm}^{-1}$, which would correspond to A_{1g} mode of WS₂, indicating the absence of sulfur doping or the sulfur concentration is negligible in the as-grown WSe₂ flakes. Moreover, we performed transmission electron microscope (TEM) and energy dispersive X-ray spectroscopy (EDX) studies. The as-grown WSe₂ flakes were first transferred onto TEM grid, using a method reported previously.⁴⁷ Figure S4 (Supporting Information) are the TEM images and a typical EDX spectrum, showing no obvious sulfur peak was found. We have acquired a few spectra from different flakes, and the results are very similar. Quantitative analysis shows that if we only count the three elements of W, Se, and S, the atomic ratio of S is below 0.5%, which is the limit of EDX technique. However, we cannot exclude the possibility that there are trace amount of sulfur-doping in as-grown WSe₂ flakes. Compared with recent papers on the growth of TMDC alloys,^{48–51} the amount of sulfur as well as its temperature were much lower in our study, which leads to the growth of WSe₂ flakes with negligible sulfur doping, if any.

We also performed Raman mapping on the same flake shown in Figure 2b. Figure 2e,f shows Raman intensity mapping images for the A_{1g} and B_{2g}¹ modes of WSe₂, respectively. As it can be clearly discerned, the areas covered by ribbons are darker than other parts. The same mapping study was performed on another flake with ribbons on top, and the results are consistent with Figure 2e,f (Supporting Information Figure S3b). This suggests that the ribbon-covered parts are thicker than other areas since both A_{1g} and B_{2g}¹ peak intensities will decrease with increasing the layer numbers of WSe₂.^{44,45} The intensity of Raman peaks are determined by the intensity of incident light and the

amount of materials involved during the scattering process. For thick WSe₂ materials, or more generally high reflective index TMDCs, the local electrical field will be much weaker than the incident electrical field, the so-called local field effect. Therefore, thick WSe₂ materials will exhibit weak Raman signal. On the other hand, for very thin WSe₂ layers, the local field effect is relatively small, and the Raman intensity will be related to the amount of materials involved during Raman scattering process.⁵² Therefore, the overall Raman intensity will be jointly determined by the local field effect and the amount of materials, and there might be a peak at certain height. In our study, we observed that the intensity of Raman peaks decreased in few-layer samples when increasing the layer numbers. This is consistent with a recent study where they showed that bilayer WSe₂ exhibit the strongest Raman intensity, and decrease in the order of 3L, 4L, and 5L.⁴⁴

AFM characterization reveals even more interesting features for stacked thick WSe₂ flakes. Figure 3a,d,e,f shows AFM phase images of four typical thick flakes with different stacking morphologies. In a more systematical AFM analysis (Supporting Information Figures S5 and S6), we found that flakes with different stacking morphologies appear at different frequencies. Among the 10 triangular flakes we examined, six of them have a 0° stacking angle, two have a 60° stacking angle, and one has a 15° stacking angle. We also checked 10 hexagonal flakes; eight of them are hexagon-triangle stacks with a 30° stacking angle, and two flakes are hexagon–hexagon stacks. These results of stacking angles and shapes are consistent with what been observed under optical microscopy (Figure 1). Moreover, steps and helical fringes were clearly observed, which strongly support the existence of screw dislocations in these WSe₂ samples. Additional

evidence like herringbone contours were also observed. Taking all the optical microscopy, AFM, and Raman observations together (Figures 1–3), we proposed that these WSe_2 flakes followed a SDD spiral growth fashion.^{40,41} In classical crystal growth theory, there are three basic growth types:^{40,41} SDD growth (BCF theory),^{53,54} layer-by-layer (LBL) growth,⁵³ and dendritic growth. The growth preference depends on the degree of supersaturation as expressed as $\sigma = \ln(c/c_0)$, where σ is the degree of supersaturation, c is the precursor concentration, and c_0 is the equilibrium concentration.^{40,41,53} At a low supersaturation (σ) condition, SDD growth is much more favorable than the other two because screw dislocations can provide active edges as nucleation sites, while LBL growth and dendritic growth require nuclei formations that occur only at certain high supersaturation conditions.

To describe the screw dislocations more quantitatively, we measured the key parameters of the screw dislocations in as-grown WSe_2 flakes, including step height (h), terrace width (λ), and slope ($p = h/\lambda$). These values can reflect the growth conditions at certain degree. In most cases, low supersaturation (σ) would result in a small p and large λ .⁴⁰ Figure 3b is a three-dimensional (3D) image of the same flake shown in Figure 3a. A pyramid-like structure with a height of 40 nm (from base to summit) is clearly observed. The height profile along the red dash line in Figure 3b is shown in Figure 3c. The step height (h) of this particular dislocation hillock is measured to be ~ 0.86 nm, which is very close to the thickness of an individual WSe_2 layer (composed to Se–W–Se layer and has a height of ~ 0.7 nm). This value is equal to one elemental Burgers vector.⁴¹ Along with the single helical pattern, we conclude that only a single screw dislocation with one elemental Burgers vector is involved in this particular flake. Other spiral growth modes with different Burgers vectors or multiple screw dislocations also exist. For example, the sample in Figure 3f has two helical patterns, which can be a result of simultaneously growth from two screw dislocations. Another important parameter, terrace width (λ), of the sample in Figure 3a,b is ~ 68 nm, which is smaller comparing to the other flakes in Figure 3d–f. From screw dislocation growth theory, the terrace width is mostly affected by the reactant concentrations. Specifically, the value of λ is determined by the lateral step velocity (ν_s) and growth rate normal to the surface (R_m). A sample grown with a relative higher R_m and smaller ν_s would display a smaller λ . And usually, a smaller λ facilitates a better observation of herringbone contours than a larger λ does. This is the reason why Figure 3a has sharp herringbone contours while the others do not. With the measured terrace width (λ) and step height (h), we can calculate that the flake shown in Figure 3a,b has a slope of $p = h/\lambda = 0.0126$. Typically, a small terrace width will lead to a high slope of the pyramid. Moreover, along

this study, we have examined tens of such spiral grown flakes and found that both clockwise and counter-clockwise grown samples with varied stacking angles exist. The different spiral features are likely to originate from the spiral growth curvature, and the spiral curvature depends much on the reactant concentrations as well. However, such concentration-curvature relation is rather complicated. In other words, the terrace width and curvature do not have direct relations. For example, in our experiments, we find flakes with the same stacking angle, but different terrace widths as shown in Supporting Information Figures S5 and S6. As the concentrations of reactants in a CVD tube furnace varies from location to location due to the use of solid precursors, this leads to the observation of many kinds of stacking morphologies on a same substrate.

To illustrate how a screw dislocation may generate, taking the situation with only one elemental Burgers vector as an example, we drew schematic diagrams to illustrate this process (Figure 4a–c). When two WSe_2 domains intersect, it can cause an uplifting of one grain boundary (Figure 4b). This process will leave some unsaturated Se atoms hanging on this uplifted edge. At this moment, latter sources can be either added to the lateral edges forming a lateral growth or to the uplifted edge forming a second layer growth. Once the second layer is extended, a screw dislocation will be created, which facilitates further spiral growth of WSe_2 following a SDD model (Figure 4c). This stage corresponds to what we have observed on those thin flakes in Figure 2a,b. Later on, among those three growth modes of LBL growth, continuous lateral growth, and SDD spiral growth, which growth type is preferred depends on the concentration of reactants. As mentioned above, according to classical crystal growth theory, SDD spiral growth is the most favorable type at low supersaturation conditions.^{40,41} For CVD growth of MoS_2 , MoO_3 and S react with each other easily, thus the concentrations of active reactants may be high enough to facilitate a large area lateral growth and few-layer LBL growth. Nevertheless, some similar uplifted second layer features also exist under certain conditions.⁴² On the other hand, it is rather different for CVD growth of WSe_2 . Due to the low reactivity of Se, Huang *et al.* found that H_2 has to be introduced to help reduce WO_3 into WO_{3-x} and to obtain monolayer dominated WSe_2 flakes.³² Here in our case, we discovered that sulfur can play a similar role as H_2 does, and it is not a requirement to have H_2 involved. Since sulfur is not a strong reducer as H_2 is, and the amount of sulfur is quite little in our case, the concentration of WO_{3-x} active source is still not high enough for other types of growth except SDD growth in our case. So in this situation, lateral growth and LBL growth are likely to be prohibited while spiral growth on screw dislocations is preferred. We also performed CVD experiments without the addition of sulfur powders, and no such WSe_2

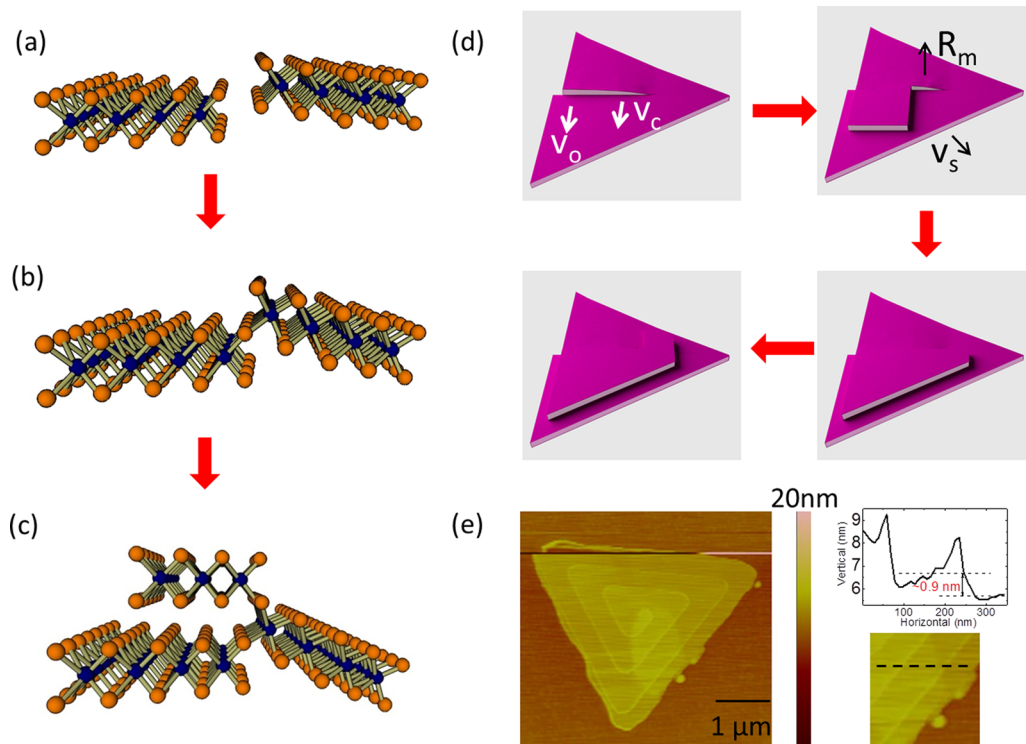


Figure 4. Proposed models for SDD growth of WSe₂. (a) Two adjacent WSe₂ domains before intersecting. (b) The boundary uplifting occurs when the two domains intersect. (c) A screw dislocation generated after the second layer extension on the uplifted edge. (d) Schematic diagrams showing the process of screw dislocation propagation. (e) AFM image of a spiral grown flake at early stage. A zoom-in image with the height profile shown in the right part.

growth was found. This is consistent with Huang *et al.*'s recent results.³²

Figure 4d illustrates how a screw dislocation propagates and eventually leads to the pyramid-like WSe₂ flake. At first with a low supersaturation environment, the step propagation velocities at the dislocation core (ν_c) and outer edges (ν_o) are approximately the same. This is evidenced by the uniformity of terrace width (λ) in AFM images. Thus, the steps can continuously spread without piling up. Moreover, the growth rate normal to the surface (R_m) is much lower than lateral step velocities (ν_s), which leads to a 2D flake instead of a 1D structure.⁴⁰ A product at the early stage with only a few terrace steps was shown in Figure 4e, which clearly reveals the early structures of screw dislocations in the samples. During the CVD growth period, the concentration of Se will decrease gradually along with the Ar flow due to the amount of Se powder left will decrease. On the basis of SDD growth theory, the terrace width will increase as the reactant concentration decreases. This may be the main reason that we frequently observe on most flakes that the terrace width increases after certain periods.

We further performed electrical transport measurements to study the electronic quality of the as-grown WSe₂ flakes. Compared to a recent study of CVD growth of WSe₂ on sapphire,³² our samples were grown directly on Si/SiO₂ substrates, which facilitates the fabrication of back-gated field-effect transistors

(FETs). The devices were fabricated using standard e-beam lithography and the electrodes were 1 nm/75 nm of Ti/Pd (see Methods for details). Figure 5a shows a device with a 2 μ m channel length on a 5 nm-thick flake and Figure 5b shows another device with a 1 μ m channel length on a 20 nm-thick flake. The $I_{ds}-V_g$ family curves are shown in each corresponding figure (Figure 5c,d). Interestingly, since Pd was used as the contacts, these devices show unipolar p-type behavior. This is different with recent results of ambipolar transport behavior of WSe₂ flakes when using Au as contact.^{14,15} The results suggest that the transport behavior of WSe₂ can be tuned by careful selection of metal contacts, as also demonstrated in MoS₂ devices.⁵⁵ The on/off current ratios of the devices are around 10⁴ to 10⁶, and effective hole mobility is about 40 cm²/(V·s). These values compared favorably with recent reported values for few-layer WSe₂.^{10,56}

CONCLUSION

In conclusion, few-layer and pyramid-like WSe₂ flakes were synthesized using a sulfur-assisted CVD method. The WSe₂ growth was proposed to follow a SDD growth process due to the low supersaturation of reactants. Sulfur was found to play an important role here as it can partially reduce the WO₃ while keeping the WO_{3-x} concentration low. Key screw dislocation features including steps, helical fringes, and herringbone contours were observed to support the spiral

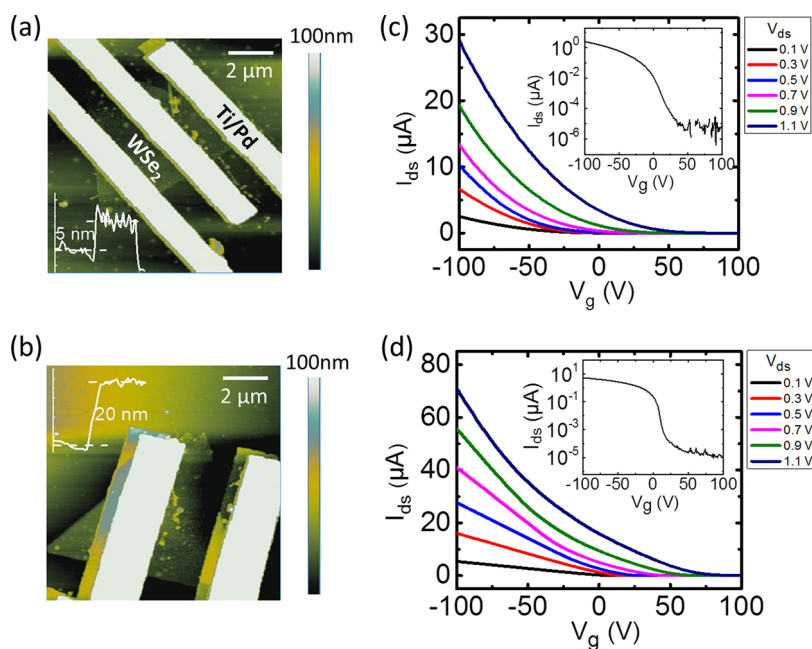


Figure 5. Device performance of CVD-grown WSe₂ flakes. (a) AFM image of a back-gated WSe₂ FET on a 5 nm-thick sample along with its I_{ds} – V_g family curves at different V_{ds} . (c) (b) Another back-gated WSe₂ FET on a 20 nm-thick sample with its I_{ds} – V_g family curves (d). Insets in the right plots (c) and (d) are transfer curves plotted in a log scale at $V_{ds} = 0.1$ V.

growth. Schematic models were drawn to illustrate how the screw dislocations generate and propagate. In addition, transistors fabricated using these WSe₂ flakes show that they possess decent device performance

with on/off current ratio up to 10^6 and hole mobility up to $44 \text{ cm}^2/(\text{V}\cdot\text{s})$. This work sheds new light on the understanding of growth mechanism of layered WSe₂, which might be also adoptable in other 2D materials.

METHODS

CVD Growth of WSe₂ Flakes. In a typical experiment, WO₃ nanopowders (40 mg, Sigma-Aldrich) were loaded in a quartz boat and put at the center of a 1-in. tube furnace. A Si/SiO₂ substrate (300 nm SiO₂) was placed on top of the quartz boat at a distance ~ 0.5 cm at the downstream of the WO₃ powders. Selenium powders (30 mg, Sigma-Aldrich) and a small amount of sulfur powders (5 mg, Sigma-Aldrich) were put at upstream with temperatures of 400 °C (for selenium) and 85 °C (for sulfur). Since the temperature was below the melting point of sulfur (115.2 °C), only very little sulfur vapor was carried to the reaction zone by a small flow of Ar gas (14 sccm). This is evident from the fact that there is still some sulfur left in the boat after the experiments. The furnace was first purged with 100 sccm of Ar for 10 min, then raised to the growth temperatures in 16 min, and kept for 12 min for WSe₂ growth. After that, it was naturally cooled down to room temperature. The flow rate of Ar was 14 sccm during the CVD process.

Characterization. The as-grown flakes were characterized by optical microscopy, Raman spectroscopy (532 nm laser, Renishaw Raman), AFM (DI 3100 Digital Instruments, tapping mode), and TEM (JEOL 2100 F, 200 kV, equipped with detector for EDX).

Device Fabrication and Measurements. The transistors were directly fabricated on Si/SiO₂ substrates where WSe₂ were grown using standard e-beam lithography. A PMMA layer was first spin-coated onto the Si/SiO₂ surface. Then, e-beam lithography was conducted to pattern source/drain electrodes, followed by developing, metal deposition, and lift-off processes. Ti/Pd electrodes (1 nm/75 nm) were deposited at 1×10^{-6} Torr using an e-beam evaporator. The device measurements were performed under Agilent 4516 in ambient condition.

Conflict of Interest: The authors declare no competing financial interest.

Acknowledgment. This work was supported by the Office of Naval Research (ONR) and the Air Force Office of Scientific Research (AFOSR). We would like to acknowledge the collaboration of this research with King Abdul-Aziz City for Science and Technology (KACST) via The Center of Excellence for Nanotechnologies (CEGN). TEM and EDX images used in this article were acquired at the Center for Electron Microscopy and Microanalysis, University of Southern California. We acknowledge Professor Stephen Cronin of University of Southern California for access to Raman facility.

Supporting Information Available: Additional AFM, TEM, EDX, and Raman results. This material is available free of charge via the Internet at <http://pubs.acs.org>.

REFERENCES AND NOTES

- Wang, Q. H.; Kalantar-Zadeh, K.; Kis, A.; Coleman, J. N.; Strano, M. S. Electronics and Optoelectronics of Two-Dimensional Transition Metal Dichalcogenides. *Nat. Nanotechnol.* **2012**, *7*, 699–712.
- Chhowalla, M.; Shin, H. S.; Eda, G.; Li, L. J.; Loh, K. P.; Zhang, H. The Chemistry of Two-dimensional Layered Transition Metal Dichalcogenide Nanosheets. *Nat. Chem.* **2013**, *5*, 263–275.
- Geim, A. K.; Grigorieva, I. V. Van der Waals Heterostructures. *Nature* **2013**, *499*, 419–425.
- Radisavljevic, B.; Radenovic, A.; Brivio, J.; Giacometti, V.; Kis, A. Single-Layer MoS₂ Transistors. *Nat. Nanotechnol.* **2011**, *6*, 147–150.
- Kuc, A.; Zibouche, N.; Heine, T. Influence of Quantum Confinement on the Electronic Structure of the Transition Metal Sulfide TSe₂. *Phys. Rev. B* **2011**, *83*, 245213.

6. Mak, K. F.; He, K.; Shan, J.; Heinz, T. F. Control of Valley Polarization in Monolayer MoS₂ by Optical Helicity. *Nat. Nanotechnol.* **2012**, *7*, 494–498.
7. Zeng, H.; Dai, J.; Yao, W.; Xiao, D.; Cui, X. Valley Polarization in MoS₂ Monolayers by Optical Pumping. *Nat. Nanotechnol.* **2012**, *7*, 490–493.
8. Pu, J.; Yomogida, Y.; Liu, K. K.; Li, L. J.; Iwasa, Y.; Takenobu, T. Highly Flexible MoS₂ Thin-Film Transistors with Ion Gel Dielectrics. *Nano Lett.* **2012**, *12*, 4013–4017.
9. Chang, H.-Y.; Yang, S.; Lee, J.; Tao, L.; Hwang, W.-S.; Jena, D.; Lu, N.; Akinwande, D. High-Performance, Highly Bendable MoS₂ Transistors with High-K Dielectrics for Flexible Low-Power Systems. *ACS Nano* **2013**, *7*, 5446–5452.
10. Tosun, M.; Chuang, S.; Fang, H.; Sachid, A. B.; Hettick, M.; Lin, Y.; Zeng, Y.; Javey, A. High-Gain Inverters Based on WSe₂ Complementary Field-Effect Transistors. *ACS Nano* **2014**, *8*, 4948–4953.
11. Wang, H.; Yu, L.; Lee, Y. H.; Shi, Y.; Hsu, A.; Chin, M. L.; Li, L. J.; Dubey, M.; Kong, J.; Palacios, T. Integrated Circuits Based on Bilayer MoS₂ Transistors. *Nano Lett.* **2012**, *12*, 4674–4680.
12. Lopez-Sanchez, O.; Lembke, D.; Kayci, M.; Radenovic, A.; Kis, A. Ultrasensitive Photodetectors Based on Monolayer MoS₂. *Nat. Nanotechnol.* **2013**, *8*, 497–501.
13. Ross, J. S.; Klement, P.; Jones, A. M.; Ghimire, N. J.; Yan, J.; Mandrus, D. G.; Taniguchi, T.; Watanabe, K.; Kitamura, K.; Yao, W.; *et al.* Electrically Tunable Excitonic Light-emitting Diodes Based on Monolayer WSe₂ p-n Junctions. *Nat. Nanotechnol.* **2014**, *9*, 268–272.
14. Pospischil, A.; Furchi, M. M.; Mueller, T. Solar-energy Conversion and Light Emission in an Atomic Monolayer p-n Diode. *Nat. Nanotechnol.* **2014**, *9*, 257–261.
15. Baugher, B. W. H.; Churchill, H. O. H.; Yang, Y.; Jarillo-Herrero, P. Optoelectronic Devices Based on Electrically Tunable p-n Diodes in a Monolayer Dichalcogenide. *Nat. Nanotechnol.* **2014**, *9*, 262–267.
16. Chang, K.; Chen, W. L-Cysteine-Assisted Synthesis of Layered MoS₂/Graphene Composites with Excellent Electrochemical Performances for Lithium Ion Batteries. *ACS Nano* **2011**, *5*, 4720–4728.
17. Hinnemann, B.; Moses, P. G.; Bonde, J.; Jørgensen, K. P.; Nielsen, J. H.; Hørch, S.; Chorkendorff, I.; Nørskov, J. K. Biomimetic Hydrogen Evolution: MoS₂ Nanoparticles as Catalyst for Hydrogen Evolution. *J. Am. Chem. Soc.* **2005**, *127*, 5308–5309.
18. Lee, Y. H.; Zhang, X. Q.; Zhang, W.; Chang, M. T.; Lin, C. T.; Chang, K. D.; Yu, Y. C.; Wang, J. T.; Chang, C. S.; Li, L. J.; *et al.* Synthesis of Large-area MoS₂ Atomic Layers with Chemical Vapor Deposition. *Adv. Mater.* **2012**, *24*, 2320–2325.
19. Ling, X.; Lee, Y. H.; Lin, Y.; Fang, W.; Yu, L.; Dresselhaus, M. S.; Kong, J. Role of the Seeding Promoter in MoS₂ Growth by Chemical Vapor Deposition. *Nano Lett.* **2014**, *14*, 464–472.
20. Wang, X.; Gong, Y.; Shi, G.; Chow, W. L.; Keyshar, K.; Ye, G.; Vajtai, R.; Lou, J.; Liu, Z.; Ringe, E.; *et al.* Chemical Vapor Deposition Growth of Crystalline Monolayer MoSe₂. *ACS Nano* **2014**, *8*, 5125–5131.
21. Zhang, Y.; Zhang, Y.; Ji, Q.; Ju, J.; Yuan, H.; Shi, J.; Gao, T.; Ma, D.; Liu, M.; Chen, Y.; *et al.* Controlled Growth of High-Quality Monolayer WS₂ Layers on Sapphire and Imaging Its Grain Boundary. *ACS Nano* **2013**, *7*, 8963–8971.
22. Coleman, J. N.; Lotya, M.; O'Neill, A.; Bergin, S. D.; King, P. J.; Khan, U.; Young, K.; Gaucher, A.; De, S.; Smith, R. J.; *et al.* Two-Dimensional Nanosheets Produced by Liquid Exfoliation of Layered Materials. *Science* **2011**, *331*, 568–571.
23. Kong, D.; Wang, H.; Cha, J. J.; Pasta, M.; Koski, K. J.; Yao, J.; Cui, Y. Synthesis of MoS₂ and MoSe₂ Films with Vertically Aligned Layers. *Nano Lett.* **2013**, *13*, 1341–1347.
24. Najmaei, S.; Liu, Z.; Zhou, W.; Zou, X.; Shi, G.; Lei, S.; Yakobson, B. I.; Idrobo, J. C.; Ajayan, P. M.; Lou, J. Vapor Phase Growth and Grain Boundary Structure of Molybdenum Disulphide Atomic Layers. *Nat. Mater.* **2013**, *12*, 754–759.
25. van der Zande, A. M.; Huang, P. Y.; Chenet, D. A.; Berkelbach, T. C.; You, Y.; Lee, G. H.; Heinz, T. F.; Reichman, D. R.; Muller, D. A.; Hone, J. C. Grains and Grain Boundaries in Highly Crystalline Monolayer Molybdenum Disulphide. *Nat. Mater.* **2013**, *12*, 554–561.
26. Lauritsen, J. V.; Kibsgaard, J.; Helveg, S.; Topsoe, H.; Clausen, B. S.; Laegsgaard, E.; Besenbacher, F. Size-Dependent Structure of MoS₂ Nanocrystals. *Nat. Nanotechnol.* **2007**, *2*, 53–58.
27. Zhu, W.; Low, T.; Lee, Y. H.; Wang, H.; Farmer, D. B.; Kong, J.; Xia, F.; Avouris, P. Electronic Transport and Device Prospects of Monolayer Molybdenum Disulphide Grown by Chemical Vapour Deposition. *Nat. Commun.* **2014**, *5*, 3087.
28. Duerloo, K. A.; Li, Y.; Reed, E. J. Structural Phase Transitions in Two-Dimensional Mo- and W-Dichalcogenide Monolayers. *Nat. Commun.* **2014**, *5*, 4214.
29. Perkins, F. K.; Friedman, A. L.; Cobas, E.; Campbell, P. M.; Jernigan, G. G.; Jonker, B. T. Chemical Vapor Sensing with Monolayer MoS₂. *Nano Lett.* **2013**, *13*, 668–673.
30. Liu, B.; Chen, L.; Liu, G.; Abbas, A. N.; Fathi, M.; Zhou, C. High-Performance Chemical Sensing Using Schottky-Contacted Chemical Vapor Deposition Grown Monolayer MoS₂ Transistors. *ACS Nano* **2014**, *8*, 5304–5314.
31. Balendhran, S.; Ou, J. Z.; Bhaskaran, M.; Sriram, S.; Ippolito, S.; Vasic, Z.; Kats, E.; Bhargava, S.; Zhuiykov, S.; Kalantar-zadeh, K. Atomically Thin Layers of MoS₂ via a Two Step Thermal Evaporation–Exfoliation Method. *Nanoscale* **2012**, *4*, 461–466.
32. Huang, J.-K.; Pu, J.; Hsu, C.-L.; Chiu, M.-H.; Juang, Z.-Y.; Chang, Y.-H.; Chang, W.-H.; Iwasa, Y.; Takenobu, T.; Li, L.-J. Large-Area Synthesis of Highly Crystalline WSe₂ Monolayers and Device Applications. *ACS Nano* **2014**, *8*, 923–930.
33. Xu, K.; Wang, Z.; Du, X.; Safdar, M.; Jiang, C.; He, J. Atomic-layer Triangular WSe₂ Sheets: Synthesis and Layer-dependent Photoluminescence Property. *Nanotechnology* **2013**, *24*, 465705.
34. Lin, Y.-C.; Lu, N.; Perea-Lopez, N.; Lin, J. L. Z.; Peng, X.; Lee, C. H.; Sun, C.; Calderin, L.; Browning, P. N.; Bresnehan, M. S.; *et al.* Direct Synthesis of van der Waals Solids. *ACS Nano* **2014**, *8*, 3715–3723.
35. Meng, F.; Jin, S. The Solution Growth of Copper Nanowires and Nanotubes Is Driven by Screw Dislocations. *Nano Lett.* **2012**, *12*, 234–239.
36. Morin, S. A.; Bierman, M. J.; Tong, J.; Jin, S. Mechanism and Kinetics of Spontaneous Nanotube Growth Driven by Screw Dislocations. *Science* **2010**, *328*, 476–480.
37. Morin, S. A.; Jin, S. Screw Dislocation-driven Epitaxial Solution Growth of ZnO Nanowires Seeded by Dislocations in GaN Substrates. *Nano Lett.* **2010**, *10*, 3459–3463.
38. Zhu, J.; Peng, H.; Marshall, A. F.; Barnett, D. M.; Nix, W. D.; Cui, Y. Formation of Chiral Branched Nanowires by the Eshelby Twist. *Nat. Nanotechnol.* **2008**, *3*, 477–481.
39. Bierman, M. J.; Lau, Y. K.; Kvit, A. V.; Schmitt, A. L.; Jin, S. Dislocation-Driven Nanowire Growth and Eshelby Twist. *Science* **2008**, *320*, 1060–1063.
40. Morin, S. A.; Forticaux, A.; Bierman, M. J.; Jin, S. Screw Dislocation-Driven Growth of Two-Dimensional Nanoplates. *Nano Lett.* **2011**, *11*, 4449–4455.
41. Zhuang, A.; Li, J. J.; Wang, Y. C.; Wen, X.; Lin, Y.; Xiang, B.; Wang, X.; Zeng, J. Screw-Dislocation-Driven Bidirectional Spiral Growth of Bi₂Se₃ Nanoplates. *Angew. Chem.* **2014**, *53*, 6425–6429.
42. Ji, Q.; Zhang, Y.; Gao, T.; Zhang, Y.; Ma, D.; Liu, M.; Chen, Y.; Qiao, X.; Tan, P. H.; Kan, M.; *et al.* Epitaxial Monolayer MoS₂ on Mica with Novel Photoluminescence. *Nano Lett.* **2013**, *13*, 3870–3877.
43. Luo, X.; Zhao, Y.; Zhang, J.; Toh, M.; Kloc, C.; Xiong, Q.; Quek, S. Y. Effects of Lower Symmetry and Dimensionality on Raman Spectra in Two-Dimensional WSe₂. *Phys. Rev. B* **2013**, *88*, 195313.
44. Li, H.; Lu, G.; Wang, Y.; Yin, Z.; Cong, C.; He, Q.; Wang, L.; Ding, F.; Yu, T.; Zhang, H. Mechanical Exfoliation and Characterization of Single- and Few-Layer Nanosheets of WSe₂, TaS₂, and TaSe₂. *Small* **2013**, *9*, 1974–81.
45. Tonndorf, P.; Schmidt, R.; Bottger, P.; Zhang, X.; Borner, J.; Liebig, A.; Albrecht, M.; Kloc, C.; Gordan, O.; Zahn, D. R.; *et al.* Photoluminescence Emission and Raman Response of

- Monolayer MoS₂, MoSe₂, and WSe₂. *Opt. Express* **2013**, *21*, 4908–4916.
46. Sahin, H.; Tongay, S.; Horzum, S.; Fan, W.; Zhou, J.; Li, J.; Wu, J.; Peeters, F. Anomalous Raman Spectra and Thickness-Dependent Electronic Properties of WSe₂. *Phys. Rev. B* **2013**, *87*, 165409.
 47. Liu, B.; Ren, W.; Gao, L.; Li, S.; Pei, S.; Liu, C.; Jiang, C.; Cheng, H. M. Metal-Catalyst-Free Growth of Single-Walled Carbon Nanotubes. *J. Am. Chem. Soc.* **2009**, *131*, 2082–2083.
 48. Li, H.; Duan, X.; Wu, X.; Zhuang, X.; Zhou, H.; Zhang, Q.; Zhu, X.; Hu, W.; Ren, P.; Guo, P.; *et al.* Growth of Alloy MoS_{2x}Se_{2(1-x)} Nanosheets with Fully Tunable Chemical Compositions and Optical Properties. *J. Am. Chem. Soc.* **2014**, *136*, 3756–3759.
 49. Mann, J.; Ma, Q.; Odenthal, P. M.; Isarraraz, M.; Le, D.; Preciado, E.; Barroso, D.; Yamaguchi, K.; von Son Palacio, G.; Nguyen, A.; *et al.* 2-Dimensional Transition Metal Dichalcogenides with Tunable Direct Band Gaps: MoS_{2(1-x)}Se_{2x} Monolayers. *Adv. Mater.* **2014**, *26*, 1399–1404.
 50. Gong, Y.; Liu, Z.; Lupini, A. R.; Shi, G.; Lin, J.; Najmaei, S.; Lin, Z.; Elias, A. L.; Berkdemir, A.; You, G.; *et al.* Band Gap Engineering and Layer-by-Layer Mapping of Selenium-Doped Molybdenum Disulfide. *Nano Lett.* **2014**, *14*, 442–449.
 51. Chen, Y.; Xi, J.; Dumcenco, D. O.; Liu, Z.; Suenaga, K.; Wang, D.; Shuai, Z.; Huang, Y.; Xie, L. Tunable Band Gap Photoluminescence from Atomically Thin Transition-Metal Dichalcogenide Alloys. *ACS Nano* **2013**, *7*, 4610–4616.
 52. Splendiani, A.; Sun, L.; Zhang, Y.; Li, T.; Kim, J.; Chim, C. Y.; Galli, G.; Wang, F. Emerging Photoluminescence in Monolayer MoS₂. *Nano Lett.* **2010**, *10*, 1271–1275.
 53. Jin, S.; Bierman, M. J.; Morin, S. A. A New Twist on Nanowire Formation: Screw-Dislocation-Driven Growth of Nanowires and Nanotubes. *J. Phys. Chem. Lett.* **2010**, *1*, 1472–1480.
 54. Burton, W. K.; Cabrera, N.; Frank, F. C. The Growth of Crystals and the Equilibrium Structure of Their Surfaces. *Philos. Trans. R. Soc., A* **1951**, *243*, 299–358.
 55. Chuang, S.; Battaglia, C.; Azcatl, A.; McDonnell, S.; Kang, J. S.; Yin, X.; Tosun, M.; Kapadia, R.; Fang, H.; Wallace, R. M.; *et al.* MoS₂ P-Type Transistors and Diodes Enabled by High Work Function MoO_x Contacts. *Nano Lett.* **2014**, *14*, 1337–1342.
 56. Allain, A.; Kis, A. Electron and Hole Mobilities in Single-Layer WSe₂. *ACS Nano* **2014**, *8*, 7180–7185.